processes

MDPI

Article

Efficient Absorption of Representative Chlorinated VOCs by Functionalized Deep Eutectic Solvents: Performance Evaluation and Mechanism Exploration

Jiayi Guo [1], Chao Chen [2,*] and Jia Wang [2,*]

[1] College of Chemical and Biological Engineering, Shandong University of Science and Technology, 579 Qianwangang Road, Qingdao 266590, China; guojiayi@sdust.edu.cn
[2] College of Materials Science and Engineering, Taiyuan University of Technology, Taiyuan 030024, China
* Correspondence: chenchao8901@126.com (C.C.); wangjia01@tyut.edu.cn (J.W.)

Abstract

The efficient capture of chlorinated volatile organic compounds (Cl-VOCs) represents a significant challenge in environmental protection and sustainable chemical engineering. In this study, a functional deep eutectic solvent (DES) composed of tetrabutylphosphonium bromide ([P_{4444}][Br]) and levulinic acid (LEV) at a 1:2 molar ratio was prepared, and its absorption performance toward two typical Cl-VOCs, namely dichloromethane (DCM) and chloroform (TCM), was evaluated using this DES as a recyclable absorbent. Based on COSMO-SAC model predictions and experimental validation, the [P_{4444}][Br]-LEV (1:2) system was identified as the preferred candidate. Under mild conditions (10 °C, N_2 flow rate of 100 mL/min), the saturated absorption capacities of this DES reached 1521.71 mg/g and 1620.30 mg/g for DCM and TCM, respectively. The absorbent exhibited favorable regeneration stability over five consecutive absorption–desorption cycles, retaining over 90% of its initial absorption efficiency. Mechanistic studies, including proton nuclear magnetic resonance (^{1}H NMR), Fourier-transform infrared spectroscopy (FT-IR), DSC (Differential Scanning Calorimetry), TGA (Thermogravimetric Analysis) and quantum chemical calculations, including electrostatic potential (ESP), independent gradient model (IGM), and reduced density gradient (RDG), demonstrated that the absorption process was dominated by physical interactions such as hydrogen bonding and van der Waals forces, with no chemical reactions involved. At the laboratory scale, this DES system showed excellent Cl-VOCs absorption performance, providing a useful reference for the rational design of high-efficiency VOC absorbents.

Keywords: dichloromethane; chloroform; functional deep eutectic solvents; reusability; physical absorption mechanism

Check for updates

Academic Editor: Andrey Voshkin

Received: 7 April 2026
Revised: 20 April 2026
Accepted: 23 April 2026
Published: 24 April 2026

Copyright: © 2026 by the authors. Licensee MDPI, Basel, Switzerland. This article is an open access article distributed under the terms and conditions of the Creative Commons Attribution (CC BY) license.

1. Introduction

Over recent decades, rapid industrial expansion has led to widespread detection of chlorinated volatile organic compounds (Cl-VOCs) in terrestrial and aquatic ecosystems [1–3], posing significant threats to environmental and biological health [4]. As representative Cl-VOCs [5], dichloromethane (DCM) and chloroform (TCM) are extensively employed in industrial solvents, pharmaceuticals, and scientific research [5,6]. Listed in the U.S.EPA's Toxic Release Inventory (TRI) [7], DCM and TCM present serious concerns due to their high volatility, atmospheric persistence, and involvement in photochemical reactions that aggravate air pollution [8]. These compounds are also associated with severe

health effects, including hepatotoxicity and central nervous system impairment [9,10], underscoring the urgent need for their efficient removal.

Several methods are available for VOC treatment, including combustion, condensation, absorption, and biological processes [3,11,12]. Absorption remains a predominant industrial technology owing to its operational simplicity, safety, and stability [13]. Traditional organic solvents have long been valued in the field of VOC absorption due to their favorable solubility, process compatibility, and mature technology. Hadjoudj et al. [14] systematically evaluated the absorption potential of high-boiling-point organic solvents for Cl-VOCs by providing thermodynamic parameters such as Henry's constants, and further examined their cyclic regeneration performance in a hybrid absorption–pervaporation process, offering a reference for the design of novel absorbents [15].

However, the high toxicity and volatility of organic solvents limit their environmental friendliness, making it difficult to meet the requirements of green chemistry [16–18]. To address these limitations, researchers developed ionic liquids (ILs) as promising alternative solvents [19]. ILs are considered promising alternatives due to their low volatility and tunable properties. Their interactions with VOCs can be understood via σ-profile and energy analysis [20], and experimental work has confirmed the high absorption efficiency and selectivity of specific ILs, such as [EMIM][BF_4], for Cl-VOCs like chlorobenzene and dichloroethane [21,22]. Nevertheless, ILs still face challenges such as high synthesis costs and insufficient cycling stability, hindering their large-scale application. Given these challenges, deep eutectic solvents (DESs) have attracted growing attention as sustainable alternative solvents [23,24]. DESs consist of straightforward mixtures of hydrogen bond donors (HBDs) and acceptors (HBAs), offering advantages such as low cost, simple preparation, and favorable biodegradability [25,26]. A series of studies has demonstrated their remarkable potential in VOC abatement, particularly in capturing hydrophobic species. As reported, the DES developed by Moufawad et al. [27] achieved an exceptional absorption enhancement factor of 60,000 for 1-decene. Meanwhile, the strategy of DCM capture with DESs was proposed and systematically investigated by Mu et al. [26], establishing a structure-activity relationship between solvent physicochemical properties and absorption performance. Villarim et al. [28] also indicated that hydrophobic DESs outperform conventional absorbents in biogas impurity purification. Furthermore, Yu et al. [29] integrated COSMO-RS with molecular dynamics simulations to enable theoretical prediction and rational design of DES absorption performance. While these studies provide important references for the construction and application of DESs [26,30], significant knowledge gaps persist regarding their systematic capture potential for chlorinated VOCs (exemplified by DCM and TCM) and the underlying interaction mechanisms. In particular, the fundamental scientific question of whether the absorption process is predominantly governed by physical interactions—including ion-dipole interactions, anion-mediated hydrogen bonding, and van der Waals forces—or proceeds through chemical pathways involving coordination bond formation or charge-transfer complexation remains insufficiently elucidated. Based on the existing research, this study selects and evaluates a series of self-synthesized amide-based absorbents and functional DESs through COSMO-SAC calculation and σ-profile analysis, rather than a large-scale screening process, to identify promising candidates for capturing two typical Cl-VOCs, namely DCM and TCM, in terms of absorption capacity and cycling stability. Particular focus is placed on a functional DES, tetrabutylphosphonium bromide-levulinic acid ([P_{4444}][Br]-LEV). To clarify the absorption mechanism, electrostatic potential (ESP), independent gradient model (IGM), and reduced density gradient (RDG) analyses are adopted, emphasizing anion-mediated interactions in functional DESs. This work aims to verify whether physical interactions dominate the absorption process. The findings are expected to reveal structure-activity relationships and mechanistic insights

for functional DESs in Cl-VOCs capture, providing a theoretical reference for the rational design of DES-based absorbents for Cl-VOC removal.

2. Materials and Methods

2.1. Materials

The chemical reagents used for preparing the DESs were purchased directly and used without further purification. Detailed information on the chemicals is provided in Table 1.

Table 1. Detailed information of chemical reagents.

Chemicals	CAS No.	Suppliers	Purity wt%
Dichloromethane	75-09-2	Shanghai Macklin Biochemical Co., Ltd., Shanghai, China	≥99.5%
Chloroform	67-66-3	Shanghai Macklin Biochemical Co., Ltd., Shanghai, China	≥99.0%
N, N-dimethylformamide	68-12-2	Shanghai Macklin Biochemical Co., Ltd., Shanghai, China	≥99.5%
1-ethyl-3-methylimidazolium tetrafluoroborate	143314-16-3	Shanghai Macklin Biochemical Co., Ltd., Shanghai, China	≥99.0%
Levulinic acid	123-76-2	Shanghai Macklin Biochemical Co., Ltd., Shanghai, China	≥99.0%
Ethylene glycol	107-21-1	Shanghai Macklin Biochemical Co., Ltd., Shanghai, China	≥99.0%
Glycolic acid	79-14-1	Chengdu Kelon Chemical Co., Ltd., Chengdu, China	≥98.0%
Glycerol	56-81-5	Shanghai Macklin Biochemical Co., Ltd., Shanghai, China	≥99.0%
Methyltributylammonium Chloride	56375-79-2	Shanghai Macklin Biochemical Co., Ltd., Shanghai, China	≥99.0%
Tetrabutylphosphonium Bromide	3115-68-2	Shanghai Macklin Biochemical Co., Ltd., Shanghai, China	≥99.0%

2.2. Preparation and Characterization of DESs

Based on the hydrogen bond self-assembly principle, a series of DESs with different compositions were prepared using the conventional heating method [22,26]. Mixtures of HBAs and HBDs at predetermined molar ratios were placed in a 20 mL glass vial and continuously stirred at 80 °C for 2–3 h until a homogeneous transparent liquid formed. The absence of phase separation or precipitation after cooling to room temperature preliminarily confirmed the successful formation of the DESs. The resulting DESs were then transferred to a rotary evaporator (Model RE-5299, Shanghai Yukang Educational Equipment Co., Ltd., Shanghai, China) for dehydration (50 °C, 80 r/min, 90 min), followed by further drying in a vacuum oven (Model DZF-6050, Zhengzhou Yuke Instrument Equipment Co., Ltd., Zhengzhou, China) at 60 °C for 12 h to remove residual trace water and volatile impurities, thereby ensuring the accuracy of subsequent experiments. The water content of the DESs was measured by Karl Fischer titration (Model HD-WS6, Shandong Horde Electronic Technology Co., Ltd., Weifang, China) and found to be below 0.85 wt%. Detailed compositions are presented in Table S1 in the Supplementary Materials.

2.3. Determination of Absorption Capacity

Absorption experiments of DCM and TCM using the as-prepared DESs were performed in a self-built equilibrium absorption setup, the detailed structure of which is illustrated in Figure S1 (Supplementary Materials) [28]. In a typical run, the nitrogen flow rate was fixed at 100 mL/min, and the carrier gas was passed through DCM or TCM

liquid to achieve sufficient contact via bubbling. The resulting vapor-laden gas was then guided through a buffer flask before entering the absorption unit. A 15 mL glass vial containing 12 mL of DES was used as the absorption vessel, and the system temperature was controlled at 10–30 °C (in 10 °C increments) using a thermostatic water bath. A polytetrafluoroethylene (PTFE) tube with an inner diameter of 3 mm was employed to introduce the gas stream, with the outlet positioned just above the DES surface to avoid disturbance and ensure stable absorption behavior [26]. The absorption vial was weighed every 10 min using an electronic analytical balance (Model FA1004T, Changzhou Xingyun Electronic Equipment Co., Ltd., Changzhou, China) with an accuracy of 0.0001 g, and the cumulative absorption capacity was calculated from the recorded mass gain.

Simultaneously, a FULI INSTRUMENTS GC9790 Plus gas chromatograph (GC, Fuli Instruments Co., Ltd., Wenling, China) was used for on-line monitoring of two key gas streams: the inlet DCM/TCM-saturated gas before absorption, and the outlet exhaust gas after passing through the DES. The capture efficiency of DES toward DCM and TCM was determined by comparing the concentrations of these two streams. Absorption was regarded as reaching saturation when the outlet gas concentration remained constant for 30 consecutive minutes. The saturated DES was subsequently regenerated via vacuum-assisted thermal desorption. Detailed GC analytical conditions are summarized in Table 2.

Table 2. GC analysis conditions.

Part	Parameter Type	Conditions
Injection port	Temperature	100 °C
	Injection volume	20 μL
	Split ratio	100:1
Detector	Type	Flame Ionization Detector (FID)
	Temperature	160 °C
Chromatographic column	Type	Capillary column
	Dimensions	SE-30 (30 m × 0.32 mm × 0.25 μm)
	Flow rate	8 mL/min
	Carrier gas	Nitrogen
Column Oven	Temperature	80 °C

Saturated absorption capacity (AC, mg/g) and absorption rate are the key parameters for evaluating the VOC absorption performance of absorbents. The absorption rate was quantitatively described using the time required to reach 90% of the saturated absorption capacity (t_{90}) as a primary kinetic indicator. The saturated absorption capacity was calculated according to Equation (1) [31].

$$\mathrm{AC} = \frac{m_2 - m_1}{m_1 - m_0} \times 1000\ (\mathrm{mg/g}) \quad (1)$$

where m_0 is the mass of the empty absorption vial, m_1 is the total mass of the DES and absorption vial before absorption, and m_2 is the corresponding total mass after absorption.

2.4. Quantitative Calculations

The intermolecular interactions between DES components and target VOCs were investigated through quantum chemical calculations. Geometry optimization of all isolated molecules and their complexes was performed using the ORCA 5.0 software package (Max Planck Institute for Coal Research, Mülheim an der Ruhr, Germany) [32] at the density functional theory (DFT) level with the B3LYP/6-311G (d,p) functional [33]. The DFT-D3 dispersion correction was included to accurately describe van der Waals interactions [34].

Wave function analyses, including ESP [35], IGM [36], and RDG analyses [37], were then carried out on the optimized structures using the Multiwfn 3.8 program (Beijing Kein Research Center for Natural Sciences, Beijing, China) [38]. Molecular structures and non-covalent interaction regions were visualized with VMD 1.9.3 (University of Illinois at Urbana-Champaign, Urbana, IL, USA) [39], while IGM isosurface plots were generated using gnuplot 5.4.2 (gnuplot Development Team, available online) [40].

3. Selection and Characterization of DESs

3.1. Preliminary Selection of DESs

Since Cl-VOC molecules such as DCM and TCM contain both C–Cl polar bonds and nonpolar carbon skeletons, with their hydrogen atoms also showing moderate HBD characteristics, efficient absorbents should be capable of both hydrogen-bonding and nonpolar interactions to achieve strong capture performance. On this basis, in combination with σ-profile analysis from the COSMO-SAC model, candidate components were selected according to typical DES design principles: quaternary ammonium or phosphonium salts as HBAs, and carboxylic acids or polyols as HBDs [41].The compatibility of these components with Cl-VOCs was further evaluated from the perspective of intermolecular interactions.

For HBD selection, eight candidates were initially chosen and classified into three groups based on their functional groups. As shown in Figure 1a, the σ-profile distributions of different HBDs differ considerably. Carboxylic acids, including acetic acid (AcOH), levulinic acid (LEV), and glycolic acid (GA), exhibit strong and concentrated peaks in the negative σ-profile region, indicating high HBD ability. This favors the formation of stable hydrogen bonds with chlorine atoms in Cl-VOCs. Meanwhile, their moderate distribution in the weakly polar region also enhances overall intermolecular association. Among these, LEV displays a wider σ-profile range, suggesting a more diverse charge distribution and stronger overall interaction potential. By comparison, polyols such as ethylene glycol (EG), glycerol (Gly), and triethylene glycol (TEG) show weaker peak intensities in the negative σ-profile region but more prominent distributions near $\sigma \approx 0$, implying stronger nonpolar interaction ability. Notably, EG exhibits a distinct peak in the nonpolar region, which matches well with the nonpolar frameworks of Cl-VOCs. Among the other components, water (H_2O) has a highly concentrated σ-profile; despite strong hydrogen-bonding character, its interaction modes are relatively simple. Urea and phenol (PhOH) display bipolar character to varying degrees and were mainly used for comparative mechanistic analysis.

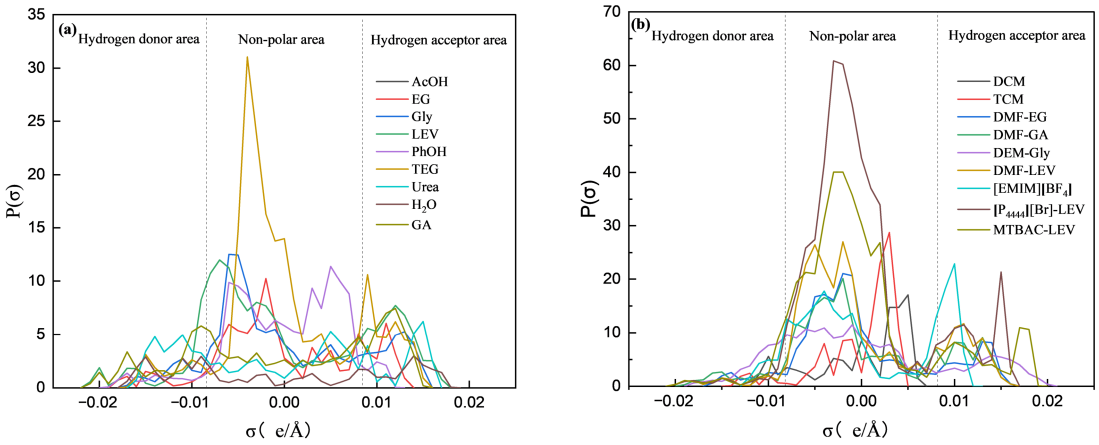


Figure 1. σ-profile diagram of (**a**) different HBDs, (**b**) different DESs.

For HBA selection, candidates were identified by comprehensively considering the absorption requirements for Cl-VOCs, the structural stability of DESs, and the HBA behaviors

reflected in the σ-profile (Figure 1b). Accordingly, [P_{4444}][Br], MTBAC (Methyltributylammonium Chloride), and DMF (N, N-dimethylformamide) were chosen as representative HBAs, corresponding to quaternary phosphonium salts, quaternary ammonium salts, and amide compounds, respectively. As shown in Figure 1b, these HBA candidates exhibit distinct distribution features in the positive σ-profile region (the HBA region). [P_{4444}][Br] presents a broad and intense peak in the positive σ-profile region, indicating strong HBA capacity. In addition, its long alkyl chains lead to a significant nonpolar contribution, which strengthens van der Waals interactions with the hydrophobic backbones of Cl-VOCs. MTBAC also shows a discernible peak in the positive σ-region, but with lower intensity and narrower range relative to [P_{4444}][Br], implying weaker HBA performance. In contrast, DMF displays a concentrated yet weak distribution in the positive σ-region, with intermolecular interactions relying mainly on lone-pair electrons of the carbonyl group, leading to a relatively limited interaction pattern.

Based on the above selection results, four amide-based DESs (DMF–LEV, DMF–EG, DMF–GA, DMF–Gly) and two functional ionic DESs ([P_{4444}][Br]-LEV and MTBAC–LEV) were prepared and further studied. Comparing their σ-profile curves reveals that the functional ionic DESs exhibit more intense charge density peaks and broader negative potential distribution in the HBA region than the amide-based DESs, along with significantly enhanced electron-donating ability. This improves their compatibility with the HBD characteristics of DCM and TCM, providing a favorable basis for the efficient Cl-VOC capture.

3.2. Characterization of DESs

In this study, a combination of proton nuclear magnetic resonance (^{1}H NMR, Figures S2 and S3), Fourier transform infrared spectroscopy (FT-IR, Figures S4 and S5), differential scanning calorimetry (DSC, Figure S6), and thermogravimetric analysis (TGA, Figure S7) was employed for multi-method characterization. Structural characterization was performed on [P_{4444}][Br]-LEV at the optimized molar ratio of 1:2, which was determined as the optimal formulation in subsequent absorption tests. Meanwhile, DMF–LEV was selected as the representative amide-based DES for structural identification, considering its superior absorption capacity among amide-type DESs as verified later. Combined with the analysis of raw material physical states, the successful formation of DESs was systematically verified from molecular structure, intermolecular interactions, and thermal properties. In particular, TGA was employed to characterize the thermal stability of the optimal absorbent [P_{4444}][Br]-LEV, further confirming its structural stability under heating conditions.

As shown in Figure S2, in the DMF–LEV (1:2) system (400 MHz, DMSO-d_6), the singlet at δ 7.95 ppm is assigned to the formyl proton (–CH=O) of DMF, while the signals at δ 2.89 and 2.73 ppm correspond to the methyl protons ($–CH_3$) of DMF. The triplets at δ 2.65 ppm (t, J = 6.5 Hz) and δ 2.38 ppm (t, J = 6.5 Hz) are attributed to the methylene protons ($–CH_2–$) of LEV, and the peak at δ 2.09 ppm corresponds to its methyl protons ($–CH_3$). All characteristic peaks are clearly assigned, and the integration ratio is consistent with the theoretical molar ratio. Meanwhile, obvious chemical shift changes are observed for the relevant protons, indicating hydrogen-bonding interactions between the two components and the formation of a stable DES system.

As shown in Figure S3, in the ^{1}H NMR spectrum (400 MHz, DMSO d_6) of [P_{4444}][Br] LEV (1:2), the peaks at δ 2.65 ppm (t, J = 6.5 Hz) and δ 2.37 ppm (dd, J = 7.0, 5.9 Hz) are assigned to the methylene hydrogens of LEV, and the singlet at δ 2.09 ppm corresponds to the methyl hydrogen of LEV. The multiplets at δ 2.26–2.14 ppm and δ 1.44 ppm are attributed to the methylene hydrogens of [P_{4444}][Br], and the triplet at δ 0.91 ppm (t, J = 7.2 Hz) belongs to its terminal methyl hydrogens. The characteristic peaks are clearly assigned, and the in-

tegration ratio matches the 1:2 stoichiometry. Obvious chemical shift changes are observed for the methylene hydrogens of the [P_{4444}][Br] cation and the characteristic hydrogens of LEV, indicating strong hydrogen bonding interactions between the phosphonium salt and LEV. The functional DES was successfully constructed, providing a structural basis for subsequent absorption performance studies.

FT-IR spectroscopy was further employed to characterize the functional group interactions within the DESs. As shown in Figure S4, the strong absorption peak of pure LEV at 1712 cm^{-1} corresponds to the C=O stretching vibration of the carboxyl group (-COOH), and the broad peak at 3000–2500 cm^{-1} is attributed to the O-H stretching vibration. For pure DMF, the peak at 1668 cm^{-1} represents the C=O stretching vibration of the amide group. After the formation of DMF-LEV, the carboxyl C=O peak of LEV red-shifted to 1705 cm^{-1}, and the O-H peak was significantly broadened with reduced intensity; the amide C=O peak of DMF also red-shifted to 1662 cm^{-1}, indicating the formation of strong hydrogen bonds between the two components and their self-assembly into a stable DES. As shown in Figure S5, after the formation of [P_{4444}][Br]-LEV (1:2), the C=O characteristic peak of LEV red-shifted to 1703 cm^{-1}, and the O-H stretching vibration shifted to lower wavenumbers with peak broadening. The P-C characteristic peaks of [P_{4444}][Br] at 1460 and 1380 cm^{-1} shifted to 1455 and 1376 cm^{-1}, respectively, confirming strong hydrogen-bonding interactions between the carboxyl group of LEV and Br^-. The FT-IR results are consistent with the ^{1}H NMR findings, providing direct experimental evidence for the successful synthesis of DESs from the perspective of functional groups.

DSC is a key thermal characterization method for verifying the successful formation of DESs, as it can distinguish simple physical mixtures from genuine DES systems through thermal behavior [42]. As shown in Figure S6, raw LEV exhibits a distinct melting endothermic peak near 20 °C, while DMF is liquid at room temperature with a melting point of −61 °C. The synthesized DMF-LEV (1:2) shows no melting peak of LEV, but only a pronounced glass transition (T_g) at −88.70 °C, with a midpoint transition temperature of −87.51 °C and a heat capacity change of 0.672 J/(g·K), indicating the formation of a homogeneous amorphous structure. Combined with the physical state change from solid LEV and liquid DMF to a uniform liquid at room temperature, this confirms that the two components form a thermodynamically stable DES through intermolecular interactions.

For the leading absorbent [P_{4444}][Br]-LEV, although DSC data are not provided, both raw materials are solids at room temperature ([P_{4444}][Br]: 100–103 °C; LEV: 30–33 °C), while their mixture forms a homogeneous liquid. This significant melting point depression is the defining feature of DESs and provides sufficient evidence for successful DES formation. To further evaluate its thermal stability under absorption and regeneration conditions, TGA was performed on [P_{4444}][Br]-LEV (Figure S7). The sample exhibits excellent thermal stability below 150 °C with negligible weight loss. Major decomposition occurs in two steps above 400 °C, corresponding to the degradation of organic components and the phosphonium salt. These results confirm that [P_{4444}][Br]-LEV possesses sufficient thermal stability for practical applications.

4. Results and Discussion

4.1. Absorption Performance of DESs

To ensure each DES was evaluated under its most stable and practical condition, amide-based DESs were initially tested at a molar ratio of 1:2, while ionic DESs were tested at 1:4 in the preliminary comparison. These ratios were selected based on preliminary formulation tests, as they provided the best stability, suitable fluidity, and moderate viscosity for each type of solvent. Single-factor experiments were conducted to evaluate the effects of HBD type, HBA/HBD molar ratio, and temperature on the absorption of DCM and TCM,

with performance compared to the conventional IL [EMIM][BF_4] [21,22]. Among the tested systems, [P_{4444}][Br]-LEV exhibited the highest absorption capacity, with saturated absorption capacities of 1363 mg/g for DCM and 1458.7 mg/g for TCM (Figure 2a). Meanwhile, the t_{90} values of [P_{4444}][Br]-LEV were 94.4 min for DCM (Figure 2b) and 108.5 min for TCM (Figure 2c), which were significantly shorter than those of other DESs and [EMIM][BF_4]. These results demonstrate that [P_{4444}][Br]-LEV showed the fastest absorption kinetics and highest mass transfer efficiency among all absorbents, significantly surpassing both [EMIM][BF_4] and the other DESs adopted in this study.

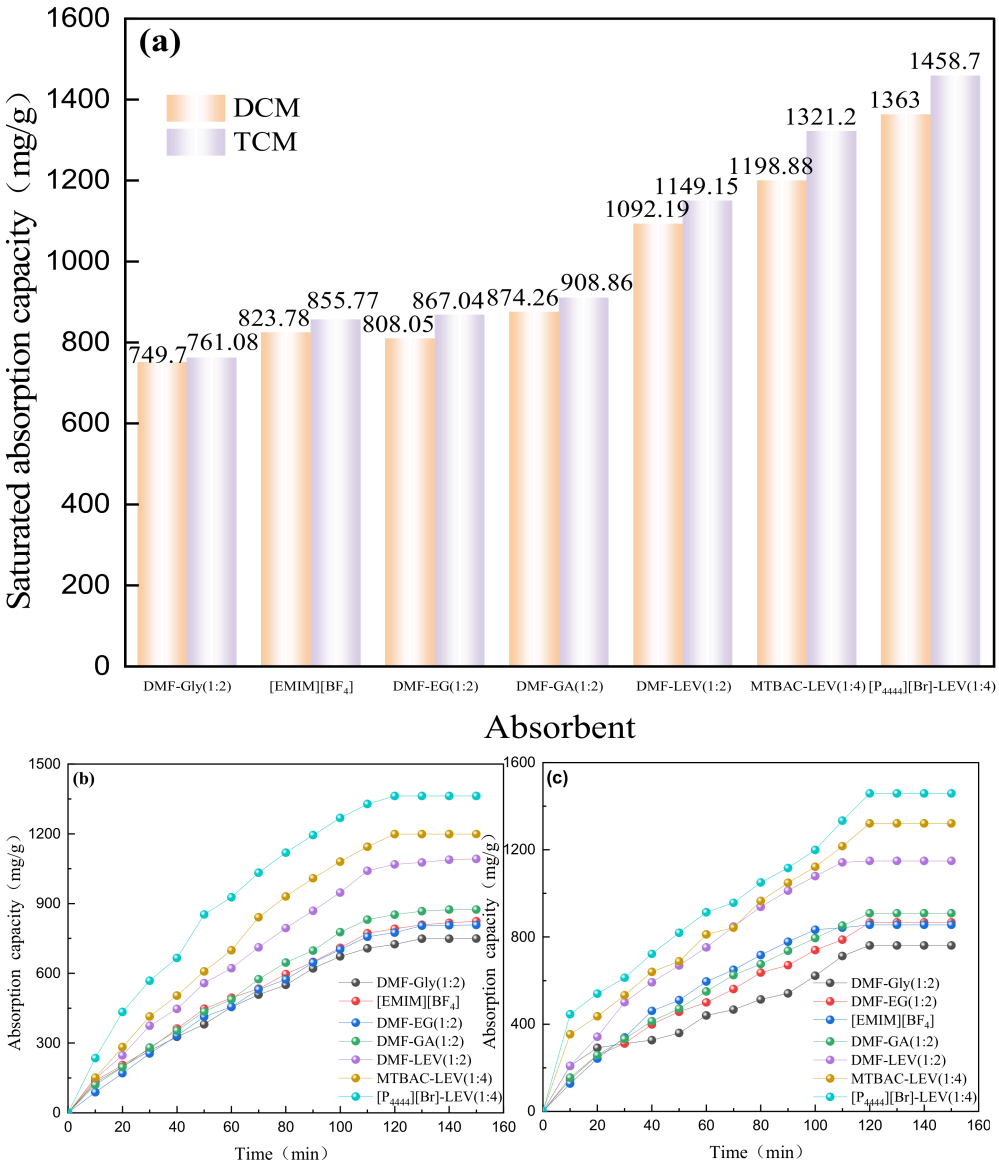


Figure 2. (**a**) Saturated absorption capacity diagram of different DESs for DCM/TCM, and absorption curves of different DESs for (**b**) DCM and (**c**) TCM.

After identifying [P_{4444}][Br]-LEV as the best-performing absorbent from preliminary screening, a systematic molar ratio optimization (1:2, 1:4, 1:6) was further conducted to clarify the influence of HBD content on absorption capacity and determine the optimal composition. Among these molar ratios, the 1:2 system achieved the highest saturated absorption capacities for DCM and TCM (Figure 3a). For DCM, the t_{90} values of [P_{4444}][Br]-LEV at molar ratios of 1:2, 1:4, and 1:6 were 97.6, 95.3, and 102.7 min, respectively. For TCM, the corresponding t_{90} values were 96.1, 108.6, and 110.1 min. Despite a negligible difference in t_{90} for DCM, the 1:2 system achieved the highest saturated absorption capaci-

ties (1521.71 mg/g for DCM and 1620.30 mg/g for TCM) and exhibited the fastest overall absorption rate, reaching saturation more rapidly (Figure 3b,c). These results demonstrate that the 1:2 system exhibits the best comprehensive performance with both high absorption capacity and fast absorption kinetics, achieving a synergistic "high-capacity and fast-absorption" effect and confirming it as the optimal molar ratio.

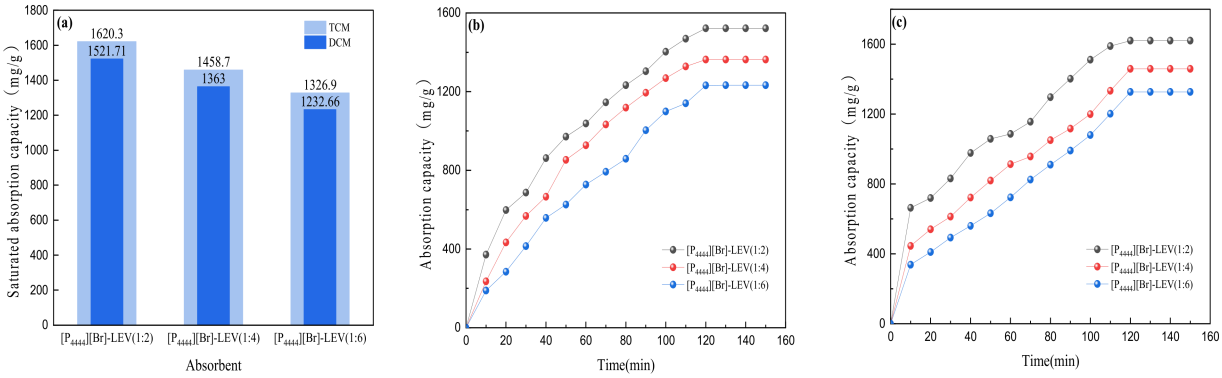


Figure 3. (**a**) Saturated absorption capacities of DCM and TCM in [P_{4444}][Br]-LEV systems with different molar ratios, and (**b**) absorption curves of DCM and (**c**) TCM in [P_{4444}][Br]-LEV systems with different molar ratios.

Based on the temperature-dependent absorption data shown in Figure 4, the saturated absorption capacities of [P_{4444}][Br]-LEV for both DCM and TCM decreased significantly as the temperature increased from 10 °C to 30 °C, with the highest capacities achieved at 10 °C (1521.71 mg/g for DCM and 1620.30 mg/g for TCM). The t_{90} values at 10, 20, and 30 °C were 96.7, 110.6, and 120.7 min for DCM, and 95.2, 101.4, and 109.9 min for TCM, respectively. The results show that the 10 °C system exhibits the shortest t_{90} values and the fastest absorption kinetics, confirming that lower temperature favors the absorption process. These observations, combined with the absence of chemical bond formation or cleavage, indicate that the absorption is dominated by physical interactions and diffusion, establishing 10 °C as the optimal temperature.

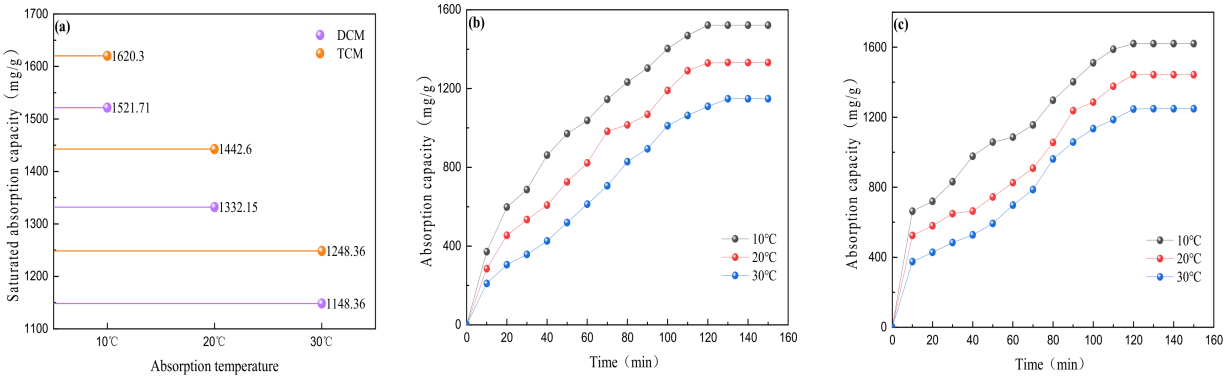


Figure 4. (**a**) Saturated absorption capacities of DCM and TCM in [P_{4444}][Br]-LEV systems at different absorption temperatures. (**b**) absorption curves of DCM in [P_{4444}][Br]-LEV systems at different temperatures. (**c**) absorption curves of TCM in [P_{4444}][Br]-LEV systems at different temperatures.

4.2. Regeneration Performance

Regeneration of the saturated [P_{4444}][Br]-LEV was achieved by vacuum-assisted thermal desorption at 80 °C and 0.6 kPa for 12 h. After five consecutive absorption–desorption cycles, the absorbent exhibited excellent regeneration stability, with retained absorption capacities of 1380.24 mg/g for DCM and 1468.24 mg/g for TCM, as shown in Figure 5.

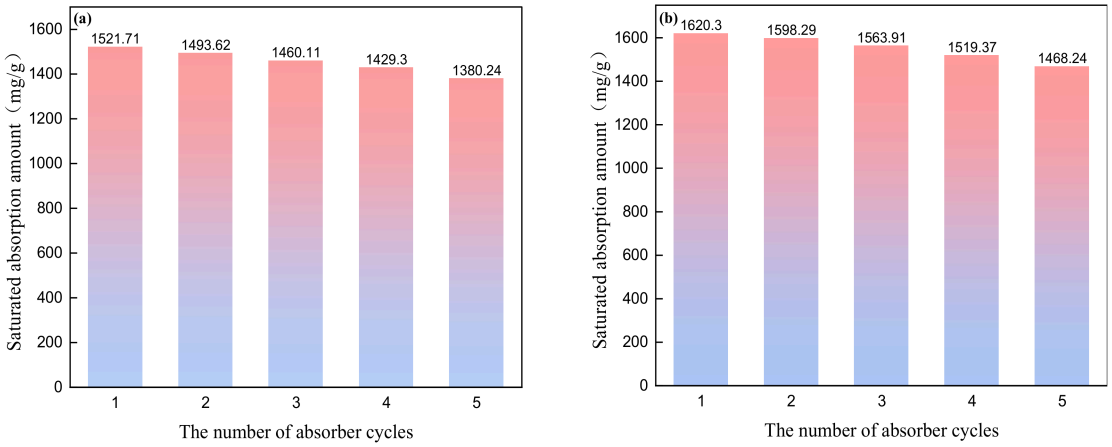


Figure 5. Changes in saturated absorption capacities of (**a**) DCM and (**b**) TCM during the cyclic process of [P_{4444}][Br]-LEV(1:2) (nitrogen flow rate of 100 mL/min, absorption temperature of 10 °C).

Fourier transform infrared spectroscopic analysis presented in Figure 6 indicates that the characteristic peaks of the [P_{4444}][Br]-LEV (1:2) system, including the C=O stretching vibrations near 1650 and 1700 cm^{-1} and the broad O-H stretching band of LEV in the 2500–3000 cm^{-1} region, remained unchanged after five consecutive absorption-regeneration cycles for both DCM and TCM. No formation of new bonds or functional groups was detected, confirming that the absorption process is physical in nature and governed primarily by van der Waals forces and hydrogen-bonding interactions. The structural integrity of the deep eutectic solvent was preserved under vacuum-assisted thermal desorption, demonstrating its stable recyclability.

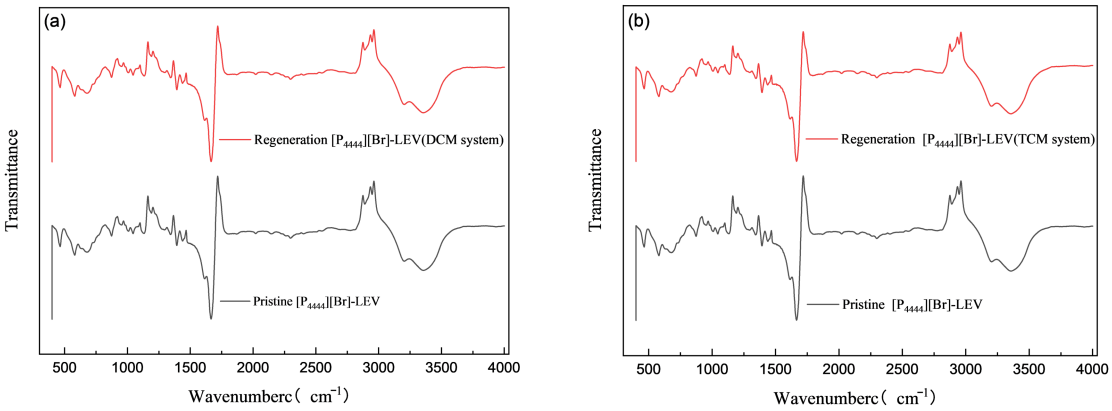


Figure 6. FT-IR spectra of pristine [P_{4444}][Br]-LEV(1:2) and regenerated [P_{4444}][Br]-LEV(1:2) after the 5th absorption of (**a**) DCM and (**b**) TCM.

4.3. Analysis of Absorption Mechanism

ESP analysis based on the van der Waals molecular surface allows precise identification of intermolecular non-covalent interaction regions [43,44]. In this work, ESP analysis (Figure 7) was performed on DCM, TCM, and the [P_{4444}][Br]-LEV system to reveal the intermolecular interaction sites from the perspective of charge distribution.

The results show that the positive electrostatic potential sites of DCM and TCM (H atoms, 28.56 and 68.33 kJ/mol, respectively) exhibit significant electrostatic potential complementarity with the negative electrostatic potential site of [P_{4444}][Br]-LEV (O in -COOH, −38.08 kJ/mol). Such spatial electrostatic matching provides microscopic evidence for intermolecular electrostatic attraction and hydrogen bond formation, essentially explaining the chemical shift deviations of characteristic protons in ^{1}H NMR and the red-shift and

broadening of carboxyl characteristic peaks in FT-IR. Furthermore, the high complementarity between the absolute negative electrostatic potential of [P_{4444}][Br]-LEV (38.08 kJ/mol) and the positive potential sites of Cl-VOCs strengthens intermolecular electrostatic interactions, which constitute the core microscopic mechanism for the superior absorption capacity of this system.

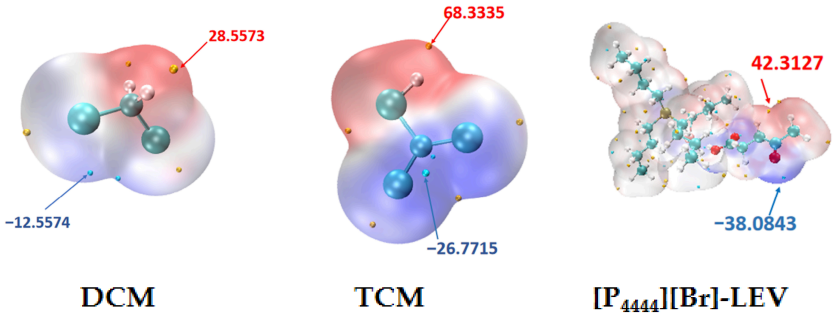


Figure 7. Molecular van der Waals surface ESP diagram of the components to be absorbed and [P_{4444}][Br]-LEV(1:2) (Red represents positive ESP, blue represents negative ESP, yellow ball represents the maximum point of ESP, and green ball represents the minimum point of ESP).

The non-covalent interaction patterns between [P_{4444}][Br]-LEV and Cl-VOCs were further elucidated using IGM and RDG analyses. These methods provided visual confirmation that the absorption mechanism is primarily driven by hydrogen bonding and van der Waals forces. Consistent with the FT-IR results, no indication of chemical bond formation or breakage was observed, further supporting the physical nature of the absorption process.

The IGM and RDG are effective tools for visualizing weak intermolecular interactions. IGM allows fragment-based analysis, minimizing intramolecular interference and providing clear spatial mapping of interaction regions [45,46]. Systematic analysis of the weak interaction regions through IGM and RDG methods, presented in Figures 8 and 9, revealed two dominant physical interaction mechanisms governing the absorption process. Distinct hydrogen-bond interactions were observed as blue-green regions in IGM plots (Figure 8), corresponding to C–H···Br^- interactions between the acidic C–H hydrogen atoms of DCM/TCM and the bromide anion of the DES. Broad green areas in RDG isosurfaces (Figure 9) indicated extensive van der Waals interactions, especially between the alkyl chains of $[P_{4444}]^+$ and Cl-VOC skeletons. The deeper blue in the TCM system (Figure 8b) reflects stronger O-H···Cl hydrogen bonds, while DCM shows C-H···Br^- hydrogen bonds alongside wider green RDG regions (Figure 9a,b), highlighting the synergy of hydrogen bonding and dispersion forces. Importantly, no red isosurfaces (indicating chemical-bond changes) appeared in IGM or RDG, consistent with FT-IR data and confirming that the absorption process is physical, governed by hydrogen bonding and van der Waals forces.

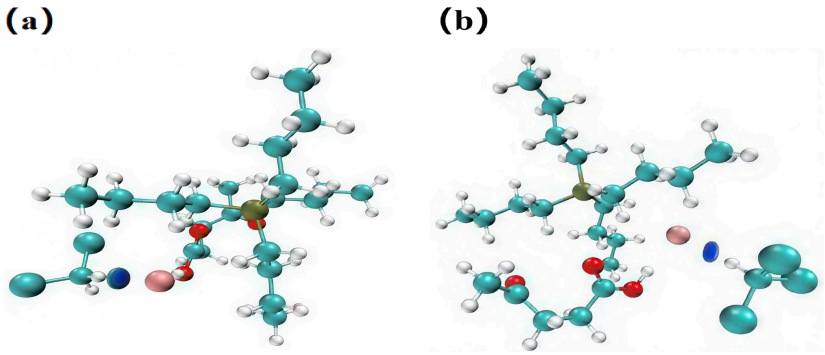


Figure 8. IGM isosurface plots of the complexes: (**a**) [P_{4444}][Br]-LEV(1:2)-DCM; (**b**) [P_{4444}][Br]-LEV(1:2)-TCM. (Blue represents strong attractive interactions such as hydrogen bonding).

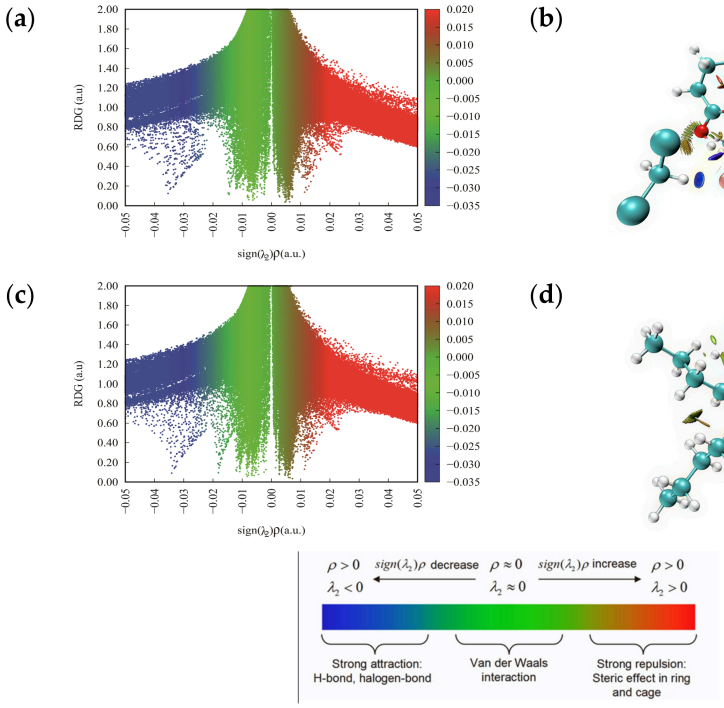


Figure 9. Scatter plots and color-filled isosurface maps of RDG analysis from wave-function calculations (**a**,**b**) [P_{4444}][Br]-LEV(1:2)-DCM system. (**c**,**d**) [P_{4444}][Br]-LEV(1:2)-TCM system. (Blue represents strong attractive interactions, green represents weak van der Waals interactions, red represents strong repulsive interactions).

5. Conclusions

This study demonstrates that the ionic DES, [P_{4444}][Br]-LEV, functions as an efficient and recyclable absorbent for Cl-VOCs, specifically DCM and TCM. Through a combined approach of COSMO-SAC screening and experimental validation, [P_{4444}][Br]-LEV (1:2) exhibited superior absorption capacities of 1521.71 mg/g for DCM and 1620.30 mg/g for TCM under mild conditions (10 °C, 100 mL/min N_2), and also achieved the fastest absorption kinetics as quantified by the shortest t_{90} values, significantly surpassing the other DESs investigated. The solvent also demonstrated excellent recyclability, maintaining over 90% of its absorption efficiency after five consecutive absorption–desorption cycles. Thermal stability analysis confirmed the structural stability of [P_{4444}][Br]-LEV above 150 °C, affirming its suitability for industrial regeneration. Combined mechanistic studies using FT-IR, ^{1}H NMR, DSC, TGA and quantum chemical calculations, specifically ESP, IGM, and RDG, confirmed a physical absorption mechanism dominated by hydrogen bonding and van der Waals interactions, with no chemical bond transformation. These results indicate that [P_{4444}][Br]-LEV is a highly efficient and recyclable absorbent for DCM and TCM capture. This work not only provides a promising candidate for Cl-VOCs removal but also offers a molecular-level strategy for the rational design of DESs in physical gas separation.

Supplementary Materials: The following supporting information can be downloaded at: https://www.mdpi.com/article/10.3390/pr14091365/s1, Figure S1: The equipment and flow chart for Cl-VOCs absorption by DESs; Figure S2: ^{1}H NMR spectrum of DMF-LEV; Figure S3: ^{1}H NMR spectrum of [P_{4444}][Br]-LEV; Figure S4: Comparison of the FT-IR spectra of DMF-LEV before and after synthesis; Figure S5: Comparison of the FT-IR spectra of [P_{4444}][Br]-LEV before and after synthesis; Figure S6: DSC curve of DMF-LEV; Figure S7: TGA curve of [P_{4444}][Br]-LEV; Table S1: All DESs prepared in this work.

Author Contributions: J.G.: Conceptualization, Methodology, Investigation, Writing—Original Draft; C.C.: Writing—Review and Editing; J.W.: Formal Analysis, Data Curation. All authors have read and agreed to the published version of the manuscript.

Funding: This research received no external funding.

Data Availability Statement: The original contributions presented in this study are included in the article/Supplementary Material. Further inquiries can be directed to the corresponding authors.

Acknowledgments: The authors would like to thank Shandong University of Science and Technology for providing the academic platform and favorable research conditions throughout this work.

Conflicts of Interest: The authors declare no conflicts of interest.

References

1. Dong, H.; Zhang, C.; Deng, J.; Jiang, Z.; Zhang, L.; Cheng, Y.; Hou, K.; Tang, L.; Zeng, G. Factors influencing degradation of trichloroethylene by sulfide-modified nanoscale zero-valent iron in aqueous solution. *Water Res.* **2018**, *135*, 1–10. [CrossRef]
2. Dutta, N.; Usman, M.; Ashraf, M.A.; Luo, G.; Zhang, S. A critical review of recent advances in the bio-remediation of chlorinated substances by microbial dechlorinators. *Chem. Eng. J. Adv.* **2022**, *12*, 100359. [CrossRef]
3. Huang, B.; Lei, C.; Wei, C.; Zeng, G. Chlorinated volatile organic compounds (Cl-VOCs) in environment—Sources, potential human health impacts, and current remediation technologies. *Environ. Int.* **2014**, *71*, 118–138. [CrossRef]
4. Li, T.; Li, H.; Li, C. A review and perspective of recent research in biological treatment applied in removal of chlorinated volatile organic compounds from waste air. *Chemosphere* **2020**, *250*, 126338. [CrossRef]
5. Gui, C.; Li, G.; Lei, Z.; Wei, Z.; Dong, Y. Experiment and molecular mechanism of two chlorinated volatile organic compounds in ionic liquids. *Ind. Eng. Chem. Res.* **2023**, *62*, 1160–1171. [CrossRef]
6. Dominguez, C.M.; Romero, A.; Lorenzo, D.; Santos, A. Thermally activated persulfate for the chemical oxidation of chlorinated organic compounds in groundwater. *J. Environ. Manag.* **2020**, *261*, 110240. [CrossRef]
7. Álvarez-Montero, M.A.; Gómez-Sainero, L.M.; Martín-Martínez, M.; Heras, F.; Rodriguez, J.J. Hydrodechlorination of chloromethanes with pd on activated carbon catalysts for the treatment of residual gas streams. *Appl. Catal. B* **2010**, *96*, 148–156. [CrossRef]
8. Kang, D.; Shi, Q.; Zhang, C.; Zhao, P.; Lyu, H.; Huang, A.; Shen, B. Modulation of acidic and redox properties of Mn-based catalysts by Co doping: Application to the synergistic removal of NO_x and chlorinated organics. *Sep. Purif. Technol.* **2024**, *339*, 126695. [CrossRef]
9. Schlosser, P.M.; Bale, A.S.; Gibbons, C.F.; Wilkins, A.; Cooper, G.S. Human health effects of dichloromethane: Key findings and scientific issues. *Environ. Health Perspect.* **2015**, *123*, 114–119. [CrossRef]
10. Thanee, K.; Youngjan, S.; Toomsan, W.; Impeng, S.; Namuangruk, S.; Butburee, T.; Rungnim, C.; Prasitnok, K.; Chawengkijwanich, C.; Khunphonoi, R.; et al. Scalable and sustainable synthesis of activated carbon-supported nanosilver with sugar and starch as dual agents for disinfection and chloroform removal. *J. Environ. Chem. Eng.* **2025**, *13*, 115526. [CrossRef]
11. Dai, C.; Zhou, Y.; Peng, H.; Huang, S.; Qin, P.; Zhang, J.; Yang, Y.; Luo, L.; Zhang, X. Current progress in remediation of chlorinated volatile organic compounds: A review. *J. Ind. Eng. Chem.* **2018**, *62*, 106–119. [CrossRef]
12. Wang, W.; Xu, Y.; Zhang, S.; Xu, Y.; Xue, X. Bibliometric insights into pollution research: Trends, geographic disparities, and emerging environmental challenges. *Environ. Res. Commun.* **2025**, *7*, 075026. [CrossRef]
13. Gui, C.; Li, G.; Zhu, R.; Lei, Z.; Dong, Y. Capturing VOCs in the pharmaceutical industry with ionic liquids. *Chem. Eng. Sci.* **2022**, *252*, 117504. [CrossRef]
14. Hadjoudj, R.; Monnier, H.; Roizard, C.; Lapicque, F. Absorption of chlorinated VOCs in high-boiling solvents: Determination of henry's law constants and infinite dilution activity coefficients. *Ind. Eng. Chem. Res.* **2004**, *43*, 2238–2246. [CrossRef]
15. Heymes, F.; Demoustier, P.M.; Charbit, F.; Fanlo, J.L.; Moulin, P. Recovery of toluene from high temperature boiling absorbents by pervaporation. *J. Membr. Sci.* **2006**, *284*, 145–154. [CrossRef]
16. Zhang, Y.; Miao, C.; Zhang, C.; Liao, Z.; Liang, C.; Yue, X.; Yan, M. Effect of ethylene glycol addition on simultaneous absorption of CO_2/H_2S by ChCl-MEA deep eutectic solvent for biomethane production. *Sep. Purif. Technol.* **2025**, *379*, 134830. [CrossRef]
17. Zheng, Q.; Liang, Z.; Li, D.; Yang, F.; Tan, H.; Wang, X. Absorption characteristics of amine-based deep eutectic solvents for CO_2 capture. *Sep. Purif. Technol.* **2025**, *378*, 134654. [CrossRef]
18. Pelaquim, F.P.; Barbosa Neto, A.M.; Dalmolin, I.A.L.; da Costa, M.C. Gas solubility using deep eutectic solvents: Review and analysis. *Ind. Eng. Chem. Res.* **2021**, *60*, 8607–8620. [CrossRef]

19. Shen, S.; Cheng, H. Rational selection and evaluation of ionic liquid as extractant for efficient separation of hexane and methyl ethyl ketone azeotrope. *Sep. Purif. Technol.* **2025**, *366*, 132699. [CrossRef]
20. Gonzalez-Miquel, M.; Palomar, J.; Rodriguez, F. Selection of ionic liquids for enhancing the gas solubility of volatile organic compounds. *J. Phys. Chem. B* **2013**, *117*, 296–306. [CrossRef]
21. Song, M.; Gui, C.; Lei, Z. Experimental and simulation studies on the capture of chlorinated volatile organic compounds by ionic liquids. *Ind. Eng. Chem. Res.* **2023**, *62*, 10184–10194. [CrossRef]
22. Mu, M.; Zhang, X.; Yu, G.; Sun, C.; Xu, R.; Liu, N.; Wang, N.; Chen, B.; Dai, C. Deep removal of chlorobenzene based volatile organic compounds from exhaust gas with ionic liquids. *Sep. Purif. Technol.* **2022**, *298*, 121610. [CrossRef]
23. Shen, Z.; Chen, L.; Cheng, H.; Qi, Z. Selective synthesis of glyceryl monolaurate intensified by boric acid based deep eutectic solvent. *Catal. Today* **2023**, *407*, 291–300. [CrossRef]
24. Wu, M.; Cheng, H.; Chen, L.; Qi, Z. Extractive deterpenation of citrus essential oils using quaternary ammonium-based deep eutectic solvents. *J. Mol. Liq.* **2021**, *336*, 116868. [CrossRef]
25. Li, G.; Gui, C.; Dai, C.; Yu, G.; Lei, Z. Molecular insights into SO_2 absorption by [EMIM][Cl]-based deep eutectic solvents. *ACS Sustain. Chem. Eng.* **2021**, *9*, 13831–13841. [CrossRef]
26. Mu, M.; Zhang, X.; Yu, G.; Xu, R.; Liu, N.; Wang, N.; Chen, B.; Dai, C. Effective absorption of dichloromethane using deep eutectic solvents. *J. Hazard. Mater.* **2022**, *439*, 129666. [CrossRef]
27. Moufawad, T.; Costa Gomes, M.; Fourmentin, S. Deep eutectic solvents as absorbents for VOC and VOC mixtures in static and dynamic processes. *Chem. Eng. J.* **2022**, *448*, 137619. [CrossRef]
28. Villarim, P.; Genty, E.; Zemmouri, J.; Fourmentin, S. Deep eutectic solvents and conventional solvents as VOC absorbents for biogas upgrading: A comparative study. *Chem. Eng. J.* **2022**, *446*, 136875. [CrossRef]
29. Yu, G.; Gajardo-Parra, N.F.; Chen, M.; Chen, B.; Sadowski, G.; Held, C. Aromatic volatile organic compounds absorption with phenyl-based deep eutectic solvents: A molecular thermodynamics and dynamics study. *AIChE J.* **2023**, *69*, e18053. [CrossRef]
30. Xu, P.; Yan, L.; Xu, Z.; Wang, Y.; Wang, L.; Sun, X.; Teng, J. Efficient capture of DMC and CO_2 in battery electrolyte VOCs with organic solvent plus ionic liquid. *Sep. Purif. Technol.* **2025**, *364*, 132397. [CrossRef]
31. Chen, H.; Feng, Z.; Yin, Z.; Wang, J.; Liu, S.; Hou, R. VOCs absorption liquid enhanced nitrogen removal in a/O reactor treating low C/N wastewater. *J. Environ. Chem. Eng.* **2025**, *13*, 118863. [CrossRef]
32. Lundgren, K.J.M.; Caldararu, O.; Oksanen, E.; Ryde, U. Quantum refinement in real and reciprocal space using the phenix and ORCA software. *IUCrJ* **2024**, *11*, 921–937. [CrossRef]
33. Chai, J.-D.; Head-Gordon, M. Long-range corrected hybrid density functionals with damped atom–atom dispersion corrections. *Phys. Chem. Chem. Phys.* **2008**, *10*, 6615. [CrossRef]
34. Grimme, S.; Antony, J.; Ehrlich, S.; Krieg, H. A consistent and accurate ab initio parametrization of density functional dispersion correction (DFT-D) for the 94 elements H-Pu. *J. Chem. Phys.* **2010**, *132*, 154104. [CrossRef]
35. Zhang, J.; Lu, T. Efficient evaluation of electrostatic potential with computerized optimized code. *Phys. Chem. Chem. Phys.* **2021**, *23*, 20323–20328. [CrossRef]
36. Lefebvre, C.; Rubez, G.; Khartabil, H.; Boisson, J.-C.; Contreras-García, J.; Hénon, E. Accurately extracting the signature of intermolecular interactions present in the NCI plot of the reduced density gradient versus electron density. *Phys. Chem. Chem. Phys.* **2017**, *19*, 17928–17936. [CrossRef]
37. Johnson, E.R.; Keinan, S.; Mori-Sánchez, P.; Contreras-García, J.; Cohen, A.J.; Yang, W. Revealing noncovalent interactions. *J. Am. Chem. Soc.* **2010**, *132*, 6498–6506. [CrossRef]
38. Lu, T.; Chen, F. Multiwfn: A multifunctional wavefunction analyzer. *J. Comput. Chem.* **2012**, *33*, 580–592. [CrossRef]
39. Humphrey, W.; Dalke, A.; Schulten, K. VMD: Visual molecular dynamics. *J. Mol. Graph.* **1996**, *14*, 33–38. [CrossRef] [PubMed]
40. Moore, B.G. Orbital plots using gnuplot. *J. Chem. Educ.* **2000**, *77*, 785. [CrossRef]
41. Liu, Q.L.; Wang, Y.; Zang, Q.J.; Wang, Z.K. Classification of deep eutectic solvents and research progress in lignin dissolution. *J. For. Chem. Ind.* **2024**, *44*, 80–90. [CrossRef]
42. Yeow, A.T.H.; Hayyan, A.; Hayyan, M.; Usman Mohd Junaidi, M.; Saleh, J.; Jefrey Basirun, W.; Nor, M.R.M.; Al Abdulmonem, W.; Salleh, M.Z.M.; Zuki, F.M.; et al. A comprehensive review on the physicochemical properties of deep eutectic solvents. *Results Chem.* **2024**, *7*, 101378. [CrossRef]
43. Yu, G.; Dai, C.; Gao, H.; Zhu, R.; Du, X.; Lei, Z. Capturing condensable gases with ionic liquids. *Ind. Eng. Chem. Res.* **2018**, *57*, 12202–12214. [CrossRef]
44. Huang, J.; Rasouli, K.; Zong, Z.; Wang, P.; Zhang, Y.; Li, Z. Engineering a high-performance ZnFe2O4/BiOBr/MXene S-scheme heterostructure for CO2 photoreduction and wastewater treatment. *Chem. Eng. J.* **2026**, *530*, 173675. [CrossRef]

45. Suja, R.; Rathika, A.; Reeda, V.S.J.; Kumar, A.A.; Divya, P. Synthesis, spectroscopic analysis (FT-IR, FT-raman, UV, NMR), non-covalent interactions (RDG, IGM) and dynamic simulation on bis(8-hydroxy quinoline) salicylate salicylic acid. *J. Mol. Struct.* **2024**, *1310*, 138231. [CrossRef]
46. Lei, Z.; Gao, H.; Yu, G.; Jiang, Y. Capturing volatile ester compounds from gas mixture with ionic liquids. *J. Mol. Liq.* **2019**, *281*, 517–527. [CrossRef]

Disclaimer/Publisher's Note: The statements, opinions and data contained in all publications are solely those of the individual author(s) and contributor(s) and not of MDPI and/or the editor(s). MDPI and/or the editor(s) disclaim responsibility for any injury to people or property resulting from any ideas, methods, instructions or products referred to in the content.